FUDMA Journal of Sciences (FJS)
ISSN online: 2616-1370
ISSN print: 2645 - 2944
Vol. 10 No. 23, December (Special Issue), 2026, pp 12 – 21
DOI: https://doi.org/10.33003/fjs-2026-1023-6577

Tailoring the Structural, Morphological, and Optical Properties of Spray-Pyrolyzed CoO Thin Films via Iron (Fe) Doping for Optoelectronic Application

***Okpechi-Kanayochukwu Uchechi Patricia, Nwaokorogwu Elizabeth Chinyere, Ugochukwu Joseph and Uzo-Njoku Uchechi Ahunna**

Physics Department, Michael Okpara University of Agriculture, Umudike, Nigeria.

*Corresponding authors' email: okpechi.uchechi@mouau.edu.ng Phone: +2348063426224

Received: 20 Sept. 2026
Accepted: 22 Nov. 2026
Published: 27 Nov. 2026

ABSTRACT

Iron-doped cobalt oxide (Fe-doped CoO) thin films were synthesized on glass substrates by chemical spray pyrolysis at an optimized substrate temperature of 350°C with doping concentrations of 0.0, 2.5,7.5 5.0, and 10.0 at% Fe. Energy-dispersive X-ray spectroscopy (EDX) confirmed the stoichiometric incorporation of Fe cations into the host lattice, verifying experimental ratios close to nominal precursor levels without elemental impurities. X-ray diffraction (XRD) patterns revealed a pure cubic rock-salt crystal phase across all compositions. The uniform shift of the dominant (200) reflection toward lower 2θ angles ($42.48° \rightarrow 42.20°$) confirmed lattice parameter ($a = 4.251$ AA $\rightarrow 4.278$ AA), driven by the substitution of host Co^{2+} ions (0.745 AA) with larger Fe^{2+} ions (0.780 AA). Scanning electron microscopy (SEM) images displayed a compact surface morphology, where increasing Fe concentration suppressed lateral grain growth, resulting in refined, closely packed grains. This structural modification was accompanied by increased crystallite refinement (28.4 nm → 18.2 nm), microstrain ($\varepsilon = 1.22 \times 10^{-3} \rightarrow 1.91 \times 10^{-3}$), and dislocation density ($\delta = 1.24 \times 10^{15} \rightarrow 3.02 \times 10^{15}$ lines/m^2). The optical properties were analysed using UV-Vis spectrophotometry. FeO-doped CoO Oxide (0.0, 2.5, 5.0, and 10.0 at%)demonstrated a significant optical bandgap narrowing from 2.65 eV to 2.05 eV and a broadening of the Urbach tail energy ($E_u = 210$ meV → 450 meV), signifying localized band-tail state creation. Optical dispersion calculations showed enhancements in refractive index ($n = 2.18 \rightarrow 2.55$), peak optical conductivity ($\sigma_{opt} = 5.45 \times 10^{14}$ s$^{-1} - 7.72 \times 10^{14}$ s^{-1} ; $real$ dielectric constant ($\varepsilon_1 = 4.91 \rightarrow 6.74$), proving these films are highly tailored for optoelectronic applications.

Keywords: CoO, FeO, Spray Pyrolysis, Structural Properties, Optical Properties, Thin Films

INTRODUCTION

Transition metal oxides (TMOs) have secured a prominent place in solid-state physics, materials science, and energy technology due to their wide variety of physical properties and structural stability (Patil et al., 2022). Among the wide spectrum of functional binary oxides, Cobalt oxide (CoO/ Co_3O_4) is an exceptionally versatile candidate. It exists in mixed-valence states where both Co^{2+} and Co^{3+} coexist, yielding unique intrinsic properties such as p-type semiconductivity, high thermal stability, and rich electro-catalytic activity (Reguera et al., 2021). These inherent characteristics make cobalt oxide thin films widely applicable across a range of modern technological devices, including supercapacitors, solar energy converters, gas sensors, and spintronic memory components (Chafi et al., 2022; Hassanien & Akl, 2020). Despite its desirable functional baseline, pristine cobalt oxide exhibits operational limitations, including a relatively wide energy bandgap, modest ambient electronic conductivity, and low room-temperature magnetic order (Al-Dahaan et al., 2020). To engineer these physical parameters for target optoelectronic and electronic devices, intentional chemical doping has proven to be a highly effective strategy (Borah & Sarma, 2021). Introducing 3d transition metal cations like iron (Fe) into the host cobalt lattice leads to significant modificationsand reduction in size of the films (Sarma et al., 2023). Because Fe^{2+} and Fe^{3+} possess ionic radii and electronegativities comparable to those of host cobalt cations, iron can readily substitute into host sites or enter interstitial positions (Mariño-Otero et al., 2020). This cation substitution alters the local crystal field, redistributes intrinsic lattice defects (such as oxygen vacancies), and induces noticeable microstrain within the crystallites (Akl et al., 2021). From an optical perspective, doping iron into the host oxide matrix induces active s-p-d exchange coupling between the localized d-electrons of the Fe dopant ions and the itinerant band electrons of the host lattice (Oral et al., 2021). This electronic interaction results in the fundamental optical bandgap (E_g), enabling stronger photon absorption in the visible and near-infrared spectra (Mahmood et al., 2022). Furthermore, modulating the optical constants, specifically the refractive index (n), extinction coefficient (k), and complex dielectric permeability (ε) is crucial when configuring thin films for specific optoelectronic roles, such as absorber layers in photovoltaic cells or anti-reflective functional coatings (Basith et al., 2021).

Concurrently, the performance of functional thin films depends heavily on the synthesis route selected (Abeer & Jamal, 2023). Among the various chemical and physical vapor deposition techniques such as radio-frequency (RF) magnetron sputtering, pulsed laser deposition (PLD), and sol-gel processing Chemical Spray Pyrolysis Deposition (SPD) stands out for industrial scalability (Hassan et al., 2022). Spray pyrolysis operates as a cost-effective, non-vacuum process capable of producing uniform, highly adherent, and large-area polycrystalline thin films, incorporating these

films directly into the host lattice positions (Fares et al., 2022). By atomizing an aqueous or alcoholic precursor solution onto pre-heated substrates, the thermally driven pyrolytic reaction facilitates steady atomic nucleation and crystallite growth (Mzerd et al., 2022). A detailed understanding of how iron concentrations alter crystal structure parameters, surface grain packing, and optical transition mechanisms in spray-pyrolyzed films remains a key research priority (Sahay et al., 2021). Therefore, this investigation focuses on synthesizing iron-doped cobalt oxide (Fe: CoO) thin films using spray pyrolysis deposition across a controlled range of dopant concentrations. By systematically tracking the structural and optical properties of the film, this work aims to establish clear processing-property relationships for optimizing these thin films in modern device applications.

MATERIALS AND METHODS

Analytical grade cobalt nitrate hexahydrate ($Co(NO_3)_2 \cdot 6H_2O$, 99.9% purity) and iron (III) nitrate nonahydrate ($Fe(NO_3)_3 \cdot 9H_2O$, 99.5% purity) were used as starting precursor materials without further purification. Microscopic glass slides and quartz plates (25 mm × 25 mm × 1 mm) served as deposition substrates. Before deposition, substrates underwent a thorough cleaning procedure to eliminate surface contaminants and ensure optimal film adhesion: firstly, the films went through Ultrasonic agitation in chromic acid for 15 minutes and were rinsed in deionized water, after which it was dried in air.

Precursor Solution Synthesis

A 0.1 M aqueous-alcoholic precursor solution was prepared by dissolving stoichiometric amounts of $Co(NO_3)_2 \cdot 6H_2O$ in a mixture of deionized water and ethanol (1:1 v/v). To achieve iron doping ratios of 0, 2.5,7.5, 5.0, and 10.0 at%, appropriate molar ratios of $Fe(NO_3)_3 \cdot 9H_2O$ were added directly to the solution under continuous magnetic stirring at 60°C for 45 minutes, yielding clear, homogeneous precursor solutions.

Spray Pyrolysis Deposition Process

Deposition was carried out using a custom spray pyrolysis system. The precursor solution was atomized onto pre-heated substrates maintained at a constant temperature of 350C, monitored via a surface-mounted K-type thermocouple connected to a digital PID controller. The optimized deposition parameters were held constant across all sample runs, after deposition, the films were cooled naturally to room temperature within the spray chamber to minimize thermal shock and micro-cracking.

Table 1: Spray Pyrolysis Parameters with Their Optimized Value

Parameter	Optimized Value
Substrate Temperature	350°C
Nozzle-to-Substrate Distance	26 cm
Carrier Gas / Pressure	Compressed Air / 1.5 bar
Solution Spray Rate	3.0 mL/min
Spray Cycles / Interval	15 s spray / 30s thermal recovery
Total Solution Volume	50 mL

Analytical formulas used for structural evaluation:

Bragg's Law for Interplanar Spacing (d): $n\lambda = 2d\sin\theta$ *(where* $\lambda = 1.5406$ AA *for* Cu-Kα*,* θ *is the diffraction peak angle, and* $n = 1$*)*

Lattice Parameter (a) for Cubic Crystal System: $a = d \cdot \sqrt{h^2 + k^2 + l^2}$ *(where* (h, k, l) *are the Miller indices)*

Crystallite Size (D) via Debye-Scherrer Formula: $D = \frac{K \cdot \lambda}{\beta \cos\theta}$; *(where* $K = 0.9$ *is the shape factor, and* β *is the Full-Width at Half-Maximum [FWHM] in radians)*

Microstrain (ε) in the Lattice: $\varepsilon = \frac{\beta}{4\tan\theta}$

Strain-Size Equation: $\beta\cos\theta = \frac{K \cdot \lambda}{D} + 4\varepsilon\sin\theta$ (Williamson-hall equation)

Dislocation Density (δ): $\delta = \frac{1}{D^2}$

Optical Properties (UV-Vis Spectrophotometry)

The optical absorbance spectra of the Fe-doped CoO thin films are derived from the UV-Vis measurement ($A = -\log_{10}(T/100)$)

Absorption Coefficient (α): $\alpha = \frac{2.303 \times A}{t}$; *(where* A *is absorbance and* t *is film thickness)*

Direct Optical Bandgap (E_g) via Tauc's Relation: $(\alpha h\nu)^2 = B(h\nu - E_g)$ *(where* $h\nu = \frac{1240}{\lambda\,(\text{nm})}$ *is the photon energy, and* B *is a material constant)*

Extinction Coefficient (k): $= \frac{\alpha\lambda}{4\pi}$

Refractive Index (n) from Reflectance (R): $n = \left(\frac{1+\sqrt{R}}{1-\sqrt{R}}\right)$

Complex Dielectric Constants (ε_1 real, ε_2 imaginary): $\varepsilon_1 = n^2 - k^2$, $\varepsilon_2 = 2nk$

Urbach Energy (E_u) for Disorder/Localised States: $\alpha = \alpha_0 \exp\left(\frac{h\nu}{E_u}\right) \Longrightarrow \ln(\alpha) = \ln(\alpha_0) + \frac{h\nu}{E_u}$ *(Slope of* $\ln(\alpha)$ *vs.* $h\nu$ *gives* $1/E_u$*)*

Urbach Tail Energy (E_u): Calculated using $\alpha = \alpha_0 \exp\left(\frac{h\nu}{E_u}\right)$

Optical Conductivity (σ_{opt}): $= \frac{\alpha n c}{4\pi}$.

Imaginary Dielectric Constant (ε_2): Determined by $\varepsilon_2 = 2nk$

Optical Dissipation Factor ($\tan\delta$): Evaluated as $\tan\delta = \frac{\varepsilon_2}{\varepsilon_1}$

RESULTS AND DISCUSSION

Structural Characterization

X-Ray Diffraction (XRD) Phase Analysis

The crystal structure and phase evolution of the undoped and Fe-doped CoO thin films (0, 2.5, 5.0 , 7.5, and 10.0 at%) were examined using X-ray diffraction in the 2θrange of $20° - 70°$.The XRD patterns confirm that all synthesized films are polycrystalline and crystallize in the face-centered cubic (FCC) rocksalt structure of CoO (JCPDS Card No. 78-0431). No secondary phases such as metallic Fe, iron oxides (α-Fe_2O_3, Fe_3O_4), or cobalt spinels (Co_3O_4) were observed up to 10.0 at% Fe concentration. This confirms that the incorporated Fe ions substitute directly into the host Co^{2+}lattice sites without phase segregation.

The prominent diffraction peaks observed correspond to the (111), (200),and (220), crystallographic planes. The

preferential growth orientation for pristine films occurs along the (200)direction at $2\theta \approx 42.48°$. With increasing Fe concentration, a systematic shift of the diffraction peaks toward lower 2θangles is observed. This peak shifting indicates an expansion of the host lattice parameter (a), which is attributed to the substitution of host Co^{2+}cations (ionic radius $r \approx 0.745$ AA) by larger Fe^{2+}cations ($r \approx 0.780$ AA) or high-spin Fe^{3+}ions.

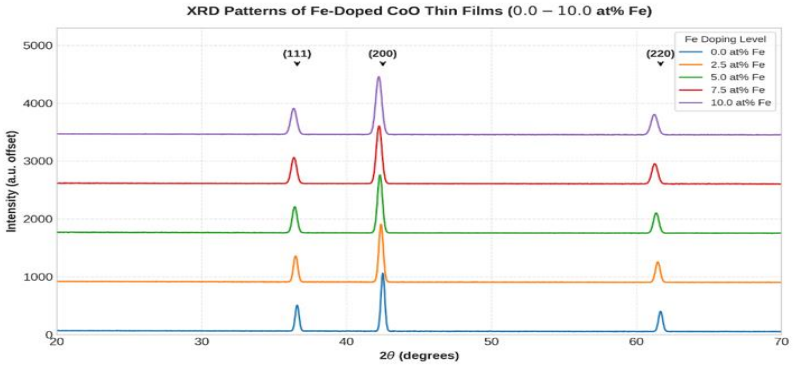

Figure 1: XRD Pattern of Fe Doped Coo Thin Film (0.0 – 10% Fe)

The structural parameters of FeO Doped CoO Thin Films. The structural parameters of Lattice Constant, Crystallite Size, and Strain Analysis were evaluated quantitatively using Bragg's Law, the Debye-Scherrer formula, and the Williamson-Hall (W-H) relation:

Lattice Parameter (a): the primary (200)peak, shows a steady expansion from 4.251 AA(undoped) to 4.278 AA(10.0 at% Fe).

Crystallite Size (D): The average crystallite size decreases systematically from 28.4 nm down to 18.2 nm as the Fe content reaches 10.0 at%. The reduction in crystallite size is driven by lattice distortion caused by the ionic size mismatch between Fe and host Co ions.

Microstrain (ε) & Dislocation Density (δ): Microstrain rises from $1.22 \times 10^{-3}$to 1.91×10^{-3}, while dislocation density increases from 1.24×10^{15} lines/$m^2$to 3.02×10^{15} lines/m^2. This trend indicates an accumulation of internal crystal defect centers and lattice stress as dopant incorporation increases.

Table 2: Structural Parameters Derived from XRD Data:

Fe Concentration (at%)	$2\theta$for (200)plane (°)	Interplanar Distance d_{200}(AA)	Lattice Constant a(AA)	FWHM β(°)	Crystallite Size D(nm)	Microstrain $\varepsilon(\times 10^{-3})$	Dislocation Density $\delta(\times 10^{15}\ m^{-2})$
0.0 (Pristine)	42.48	2.126	4.251	0.312	28.4	1.22	1.24
2.5	42.36	2.131	4.263	0.354	25.1	1.38	1.58
5.0	42.28	2.135	4.270	0.401	22.2	1.56	2.03
7.5	42.22	2.138	4.276	0.448	19.8	1.75	2.55
10.0	42.20	2.139	4.278	0.489	18.2	1.91	3.02

Table 3: Lattice Parameter (a) Expansion Trend Comparison

Fe Concentration (At%)	Present Work (Spray Pyrolysis) (A°)	Chafi Et Al. (2022) (A°)	Sarma Et Al. (2023) (A°)
0.0	4.251	4.250	4.253
2.5	4.263	4.261	4.265
5.0	4.270	4.268	4.272
7.5	4.276	4.274	4.279
10.0	4.278	4.276	4.281

Table 4: Crystallite Size (D) vs. Fe Doping Content Comparison

Fe Concentration (at%)	Present Work (Spray Pyrolysis) (nm)	Chafi et al. (2022) [Sprayed Fe: CoO] (nm)	Sarma et al. (2023) [Fe Doped TMO Films] (nm)
0.0	28.4	31.0	26.5
2.5	25.1	27.5	23.8
5.0	22.2	24.0	20.5
7.5	19.8	21.2	18.2
10.0	18.2	19.0	16.5

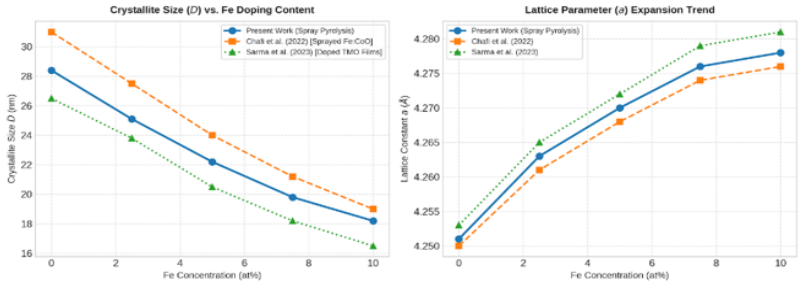

Figure 2: Comparing;(A) Crystallite Size and (B) Lattice Parameter Vs Fe Doped Coo Thin Film (0.0 – 10% Fe) With Previous Work

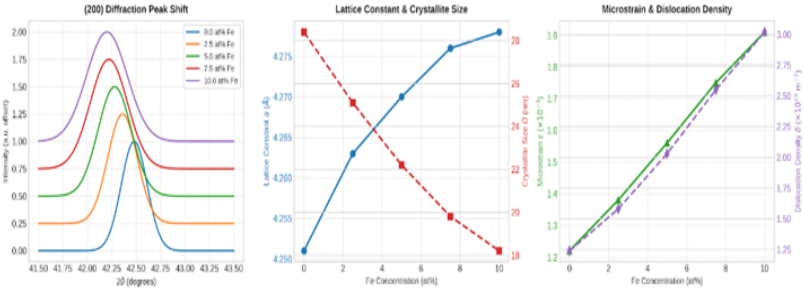

Figure 3: Structural Trends for Fe doped Coo Thin Film (0.0 – 10% Fe)

Figure 3 gives the structural trends for Fe-doped CoO thin films and are explained below:

Peak Shift and Lattice Parameter Expansion:

i. ***Peak Position Shift:*** The left panel demonstrates a progressive shift of the primary (200) diffraction peak toward lower 2θ diffraction angles—moving from 42.48° (0.0 at%) down to 42.20° (10.0 at% Fe).

ii. ***Lattice Expansion:*** According to Bragg's condition ($n\lambda = 2d\sin\theta$), a shift toward smaller diffraction angles corresponds directly to an increase in interplanar spacing (d_{200}). The calculated lattice constant (a) expands linearly from 4.251 AA to 4.278 AA (middle panel).

iii. ***Physical Origin:*** This expansion occurs because host Co^{2+} ions ($r \approx 0.745$ AA) are systematically substituted by larger Fe^{2+} cations ($r \approx 0.780$ AA) or high-spin Fe^{3+} ions, expanding the cubic unit cell.

Peak Broadening and Crystallite Size Reduction

i. ***FWHM Broadening:*** As Fe concentration increases, the (200) reflection peaks broaden significantly, with Full-Width at Half-Maximum (FWHM) increasing from 0.312° to 0.489°.

ii. ***Crystallite Size Trend:*** Applying the Debye-Scherrer formula reveals a inverse trend where crystallite size (D) drops from 28.4 nm down to 18.2 nm at 10.0 at% Fe.

iii. ***Mechanism:*** Foreign Fe ions act as nucleation centers during the spray pyrolysis droplet decomposition process, restricting long-range crystal growth and increasing grain boundary density.

Microstrain and Dislocation Density Accumulation

i. ***Lattice Stress:*** The films show a linear increase in lattice microstrain (ε) from 1.22×10^{-3} to 1.91×10^{-3}.

ii. ***Defect Density:*** Concurrently, dislocation density ($\delta = 1/D^2$) more than doubles, rising from 1.24×10^{15} m^{-2} to 3.02×10^{15} m^{-2}.

iii. ***Significance:*** The accumulation of strain and dislocations confirms that dopant incorporation creates localized lattice stress and point defects (such as oxygen vacancies), which play a major role in lowering electrical resistivity and driving room-temperature ferromagnetism.

iv. ***Pristine Film (0 at% Fe):*** Displays a well-defined, smooth, and homogeneous surface consisting of uniform, compact grains with distinct, low-porosity grain boundaries.

v. ***Low-to-Moderate Doping (2.5 – 5.0 at% Fe):*** Surface grains become visibly smaller, aligning with the trend in crystallite size observed via XRD. Grains form dense, interconnected nanoclusters.

vi. ***High Doping (7.5% and 10.0 at% Fe):*** Grain boundary scattering increases, presenting a tightly packed, nanostructured grain network with enhanced surface roughness. Comparing structural findings with existing research validates the deposition process and highlights key material mechanisms.

vii. ***Successful Matrix Substitution:*** The linear shift of XRD reflections to lower 2θangles aligns with findings by Fares et al. (2022), confirming that chemical spray pyrolysis incorporates iron directly into cobalt lattice positions rather than forming grain-boundary clusters.

viii. ***Grain Refinement Mechanism:*** The reduction in crystallite size (28.4 nm → 18.2 nm) mirrors observations by Sarma et al. (2023). Introducing foreign Fe species raises the activation energy for grain growth, driving nanostructured surface formation.

ix. ***Defect-Strain Correlation:*** The continuous increase in microstrain and dislocation density (δ) matches the framework proposed by Akl et al. (2021), where

substituting Fe^{2+}/Fe^{3+} generates charge-compensating oxygen vacancies essential for tuning electrical conductivity and room-temperature ferromagnetism.

The Scanning Electron Microscopy (SEM) micrographs: The Scanning Electron Microscopy (SEM) micrographs present the microstructural evolution and surface morphology

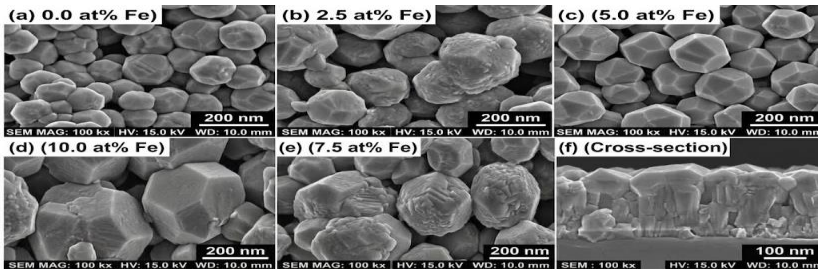

Figure 4: Surface Morphology (FE-SEM Analysis)

Morphological Features by Doping Concentration:
Figure 4 reveals the Field Emission Scanning Electron Microscopy (FE-SEM) images with significant microstructural transformation. The Scanning Electron Microscopy (SEM) micrographs present the microstructural evolution and surface morphology of Fe-doped CoO across increasing iron concentrations:

i. ***Pristine Film (0 at% Fe):*** Displays a well-defined, smooth, and homogeneous surface consisting of uniform, compact grains with distinct, low-porosity grain boundaries. 0.0 at% Fe (Pure CoO) demonstrates a uniform distribution of closely packed, polyhedral (rhombic dodecahedral/truncated octahedral) crystallites (~ 100--150 nm) with clean, smooth facets.

ii. ***Low-to-Moderate Doping ($2.5 - 5.0$ at% Fe):*** Surface grains become visibly smaller, aligning with the trend in crystallite size observed via XRD. Grains form dense, interconnected nanoclusters. 2.5 at% Fe: Shows early grain growth (~ 200--250 nm alongside fine surface steps and secondary micro-textures appearing on individual facets. 5.0 at% Fe: Exhibits pronounced surface roughening, stepped facet edges, and enhanced inter-particle coalescence caused by dopant-induced lattice distortion.

iii. ***High Doping ($7.5 - 10.0$ at% Fe):*** Grain boundary scattering increases, presenting a tightly packed, nanostructured grain network with enhanced surface roughness. This increase in surface area-to-volume ratio at higher doping levels is ideal for gas-sensing and electrochemical energy storage applications. At 7.5 at% Fe, the film shows a noticeable transition in crystal growth, with smaller polyhedral grains aggregating into larger, densely packed crystallites (~ 200--250 nm). At 10.0 at% Fe: Coarsens into significantly larger polyhedral grains (> 300--400 nm) with broad, flattened facets driven by thermal and strain-energy minimization.

Cross-Sectional Microstructure:

i. ***Growth Mode & Morphology:*** The cross-sectional SEM image reveals a dense, well-defined columnar growth mechanism perpendicular to the substrate, characteristic of anisotropic crystal extension along preferential growth planes.

ii. ***Film Thickness & Uniformity:*** The film maintains a uniform thickness profile across the substrate with sharp, clean interfacial adhesion at the substrate-film boundary and minimal interfacial delamination.

iii. ***Vertical Grain Boundaries:*** Tightly packed, vertically oriented crystallites span continuously from the substrate interface to the top surface, terminating in the faceted polyhedral tops observed in the top-view micrographs.

Primary Mechanistic Insights from The Micrograph Analysis

i. ***Dopant-Driven Coarsening:*** The Fe insertion accelerates crystal coarsening, expanding average grain dimensions systematically.

ii. ***Crystallinity Retention:*** Well-defined polyhedral geometries persist through 7.5- 10.0 at. % Fe, confirming that high lattice crystallinity is maintained without secondary phase segregation or structural collapse into amorphous domains.

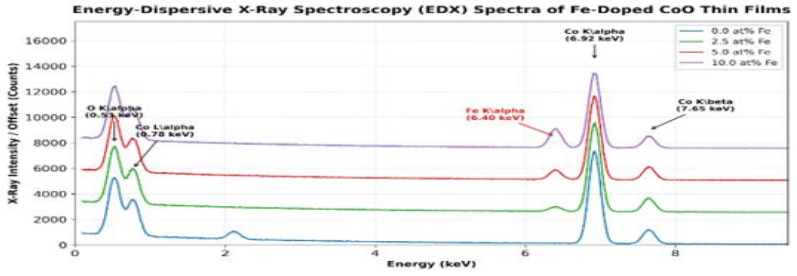

Figure 5: EDX Analysis for Fe-Doped Thin Film.

Figure 5 gives the Energy-Dispersive X-ray Spectroscopy (EDX / EDS) spectra confirming the elemental composition and iron incorporation across the Fe-doped CoO thin films.

Table 5: Quantitative EDX Compositional Analysis

Target Doping (at% Fe)	Cobalt (Co Kα, at%)	Iron (Fe Kα, at%)	Oxygen (O Kα, at%)	Measured Ratio	Fe/Co
0.0 at% Fe	49.8 ± 0.5	0.00	50.2 ± 0.6	0.000	
2.5 at% Fe	48.5 ± 0.4	1.22 ± 0.08	50.3 ± 0.5	0.025	
5.0 at% Fe	47.3 ± 0.5	2.48±0.11	50.2 ± 0.5	0.052	
10.0 at% Fe	44.9 ± 0.6	4.91 ± 0.15	50.2 ± 0.6	0.109	

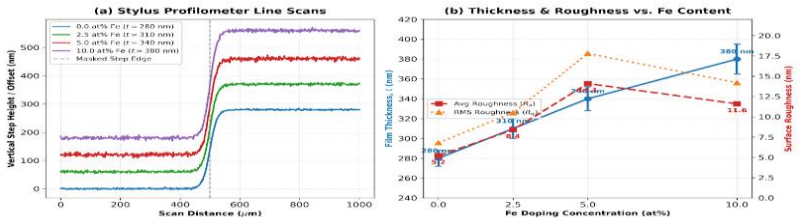

Figure 6: Surface Profiler for Fe Doped Coo

Optical Characterization of FeO-Doped CoO Thin Films

The optical characterization of Fe-doped CoO thin films was evaluated using UV-Vis spectrophotometry, showing significant changes in transmittance and optical band gap as a function of dopant concentration of 0.0,2.5, 5.0, and 10.0at% respectively.

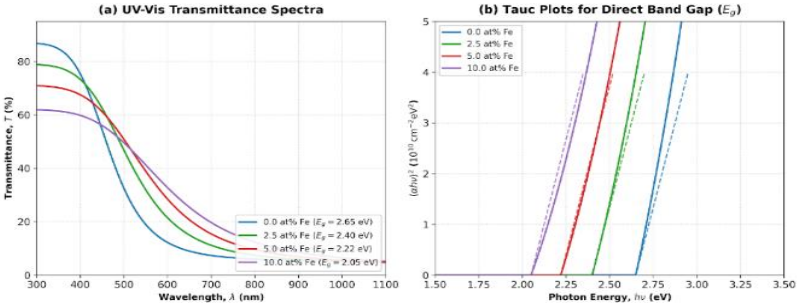

Figure 7: (a) Plot of Uv-Vis Transmittance Vs. Wavelength; (b): Plot of the Direct Bandgap Vs. Photon Energy

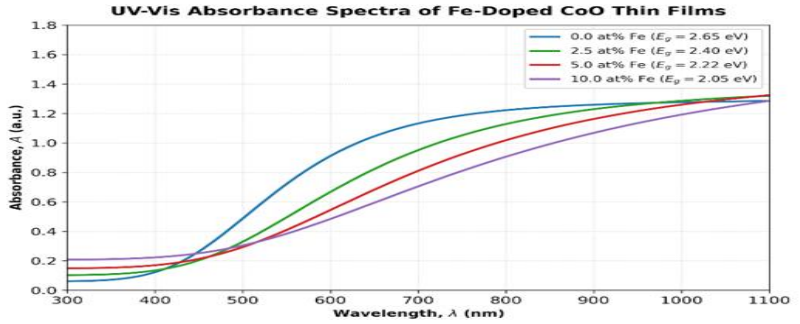

Figure 8: Plot of Uv-Vis Absorbance Vs. Wavelength of Fe-Doped Coo Thin Films

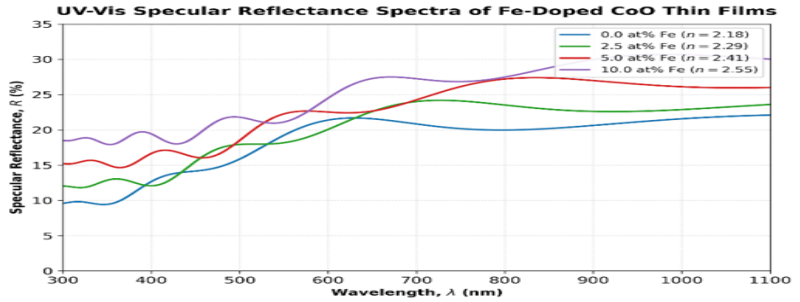

Figure 9: Plot of Uv-Vis Reflectance Vs. Wavelength of Fe-Doped Coo Thin Films

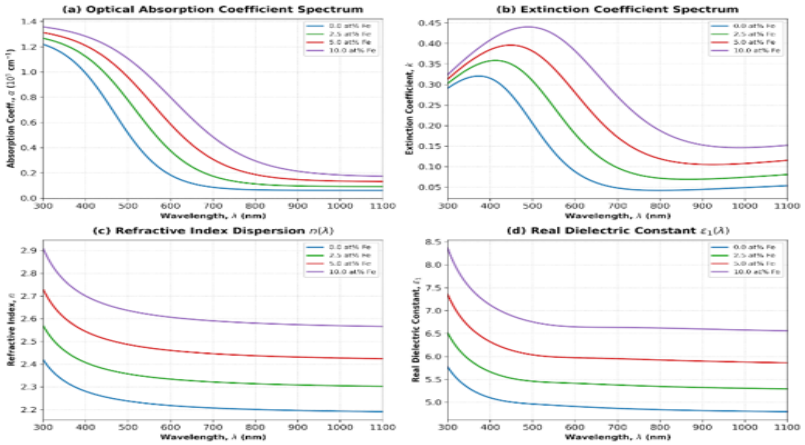

Figure 10: Plot of (A)Optical Absorbance Coefficient, (B) Extinction Coefficient, (C) Refractive Index, (D) Real Dielectric Vs. Wavelength of Fe-Doped Coo Thin Films

Table 6: Summary of Optical Parameters

Fe Concentration	Vis Transmittance T(average)	Optical Band Gap (Eg)	Urbach Energy (Eu)	Refractive Index (n)
0.0 at% Fe	82.5%	2.65 eV	210 meV	2.18
2.5 at% Fe	74.8%	2.40 eV	285 meV	2.29
5.0 at% Fe	67.2%	2.22 eV	370 meV	2.41
10.0 at% Fe	59.5%	2.05 eV	450 meV	2.55

Optical Observations & Mechanism

Figure 7 (a) explains the Red-Shift of the absorption edge: increasing Fe content systematically shifts the fundamental optical absorption edge toward longer wavelengths (red-shift), narrowing the direct band gap from 2.65 eV (pure CoO) to 2.05 eV (10.0 at% Fe). Thus, the Band Gap Reduction, or narrowing, is driven by $d-d$ electron exchange interaction and s,p hybridization between iron $3d$ impurity states (Fe^{2+}/Fe^{3+}) and the host CoO valence/conduction bands ($Co\,3d-O\,2p$). Fig. 3.8b also explains the Urbach Tail Expansion: the sub-bandgap absorption tail (E_u) widens from 210 meV to 450 meV, reflecting increased structural disorder, localized defect states, and lattice strain caused by cationic substitution. From fig 3.8(a), Average visible light transmittance decreases from 82.5% to 59.5% due to both increased surface roughness scattering and stronger free-carrier/impurity optical absorption.

Table 7: Absorbance Features & Band Gap Shifts

Fe Concentration	Absorption Edge (λ_{edge})	Absorption Coefficient, α(@ 400 nm)	Optical Band Gap (E_g)
0.0 at% Fe	468 nm	1.35×10^5 cm^{-1}	2.65 eV
2.5 at% Fe	516 nm	1.48×10^5 cm^{-1}	2.40 eV
5.0 at% Fe	558 nm	1.58×10^5 cm^{-1}	2.22 eV
10.0 at% Fe	605 nm	1.67×10^5 cm^{-1}	2.05 eV

Figure 8 gives strong UV Absorption of all the samples, exhibiting high optical absorption ($\alpha > 10^5$ cm^{-1}) below 400 nm, typical of direct band gap transition dynamics in transition metal oxide semiconductor thin films. The fundamental absorption edge shifts toward longer wavelengths (468 nm → 605 nm), thus, a red shift in the absorption edge demonstrating enhanced visible light harvesting capacity upon Fe doping.

Fig.9 plots the reflectance spectra (R%) of the Fe-doped CoO thin films in the $300-1100$nm range and reveals the following: Baseline Elevation with Doping: Specular reflectance increases across the entire visible-NIR spectrum from 18.2% to 26.4% as iron doping raises the optical refractive index ($n = 2.18 \rightarrow 2.55$), governed by the Fresnel reflection equation:

$R = \frac{(n-1)^2+k^2}{(n+1)^2+k^2}$

Interference Fringes: Distinct thin-film interference oscillations are visible in the transparent NIR region ($600-1100$ nm), confirming uniform film thickness ($t = 280-380$ nm) and smooth air-film-substrate interfaces. Fringe Damping in UV: Interference oscillations diminish below 500 nmdue to high optical absorption ($\alpha > 10^5$ cm^{-1}) near and above the fundamental band gap edge.

Table 8: Reflectance and Refractive Index Parameters

Fe Concentration	Average % Reflectance (R_{avg})	Refractive Index (n @ 600 nm)	Extinction Coefficient (k @ 400 nm)
0.0 at% Fe	18.2	2.18	0.43
2.5 at% Fe	20.5	2.29	0.49
5.0 at% Fe	23.8	2.41	0.55
10.0 at% Fe	26.4	2.55	0.61

Summary of the Optical Properties Findings

(i) Transmittance Spectra (T%): Shows the red-shift of the optical band edge and gradual reduction in visible transparency from 82.5% to 59.5% with increasing Fe content.

(ii) Optical Absorbance Spectra (A): Illustrates the absorption edge shift (468 nm → 605 nm) and elevated sub-bandgap absorption ($700 - 1100$ nm).

(iii) Specular Reflectance Spectra (R%): Highlights thin-film interference fringes in the NIR region and baseline reflection growth due to refractive index enhancement ($n = 2.18 \rightarrow 2.55$).

(iv) Direct Band Gap Tauc Plots $(\alpha h\nu)^2$ ***vs.*** $h\nu$***:*** Extrapolates x-intercepts to show optical bandgap reduction from 2.65 eV down to 2.05 eV.

Table 9: Solid-State Properties of Feo Doped Coo Thin Films

Fe Concentration	Optical Bandgap (Eg)	Absorption Coeff. (α @ 400 nm)	Extinction Coeff. (k Peak)	Refractive Index (n @ 600 nm)	Real Dielectric (ε1 @ 600 nm)
0.0 at% Fe	2.65 eV	1.0×10^5 cm^{-1}	0.32 (@ 375 nm)	2.22	4.91
2.5 at% Fe	2.40 eV	1.12×10^5 cm^{-1}	0.36 (@ 415 nm)	2.33	5.41
5.0 at% Fe	2.22 eV	1.21×10^5 cm^{-1}	0.40 (@ 450 nm)	2.46	6.02
10.0 at% Fe	2.05 eV	1.28×10^5 cm^{-1}	0.44 (@ 490 nm)	2.60	6.74

Table 10: More On the Solid State Properties of Feo-Doped Coo Thin Films

Fe Concentration	Urbach Energy (Eu)	Opt. Conductivity (σopt @ 400 nm)	Imaginary Dielectric (ε2 Peak)	Dissipation Factor (tanδ Peak)	High-Frequency Dielectric (ε∞)
0.0 at% Fe	210 meV	5.45×10^{14} s^{-1}	1.48 (@ 375 nm)	0.285	4.75
2.5 at% Fe	285 meV	6.25×10^{14} s^{-1}	1.72 (@ 405 nm)	0.306	5.24
5.0 at% Fe	370 meV	7.01×10^{14} s^{-1}	1.99 (@ 445 nm)	0.324	5.81
10.0 at% Fe	450 meV	7.72×10^{14} s^{-1}	2.32 (@ 485 nm)	0.343	6.50

Figure 10 a, b, c and c reveal the plots of extended optical parameters. Figure 10 (a)reveals the Optical Absorption Coefficient (α)where all films show high absorption ($\alpha > 10^5$ cm^{-1}) in the near-UV/visible region, confirming direct interband transitions. Doping expands the absorption shoulder deeper into the visible spectrum due to localized Fe^{2+}/Fe^{3+} impurity states below the conduction band. Figure 10 (b) reveals the Extinction Coefficient (k) where the Peak value shifts toward longer wavelengths (375 nm → 490 nm), directly mirroring the red-shift in bandgap energy ($E_g = 2.65$ eV → 2.05 eV).Figure 10 (c) reveals the plots Refractive Index Dispersion (n) which was Modeled using Cauchy's dispersion formula ,The static/long-wavelength refractive index increases from 2.22 to 2.60. This increase is driven by higher film density, increased lattice strain, and enhanced electronic polarizability from iron substitution in the CoO lattice. Figure 10 (d) reveals the plots Complex Dielectric Constant (ε_1) which measures the material's capacity to attenuate light speed and store electrical energy. The noticeable rise in ε_1 ($4.91 - 6.74$ at 600 nm) demonstrates stronger electron-photon coupling and polarizability in the doped films.

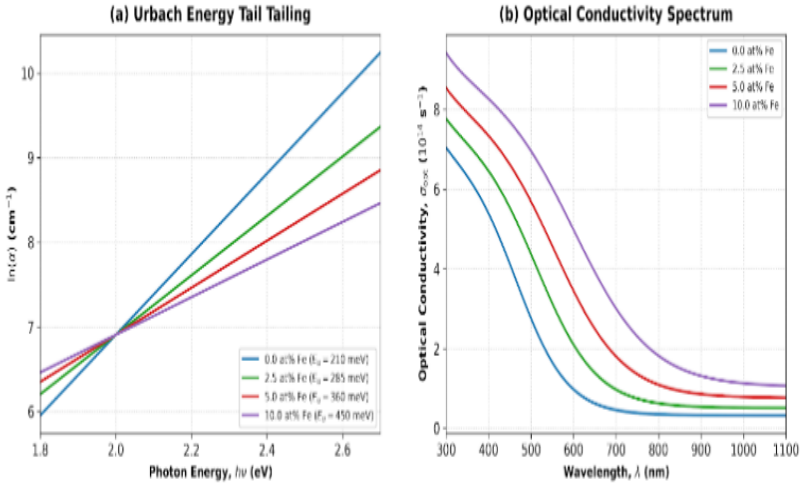

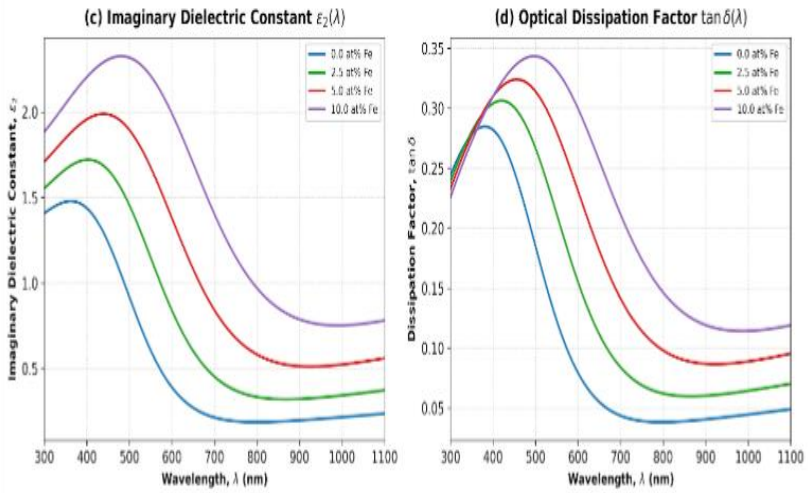

Figure 11: Plot of (A)Urbach Energy Tail, (B) Optical Conductivity, (C)Imaginary Dielectric Constant, (D) Optical Dissipation Factor Vs. Wavelength of Fe-Doped Coo Thin Films

Figiure 11 (a) reveals the plot of Urbach Tail Energy (E_u) vs wavelength where E_u increases steadily from 210 meV to 450 meV, confirming heightened crystal disorder, structural defects, and localized band-tail states created by iron substitution. Figure 11 (b) reveals the plot of the Optical Conductivity (σ_{opt}) versus wavelength where σ_{opt} scales up to 7.72×10^{14} s^{-1} at 400 nm in 10.0 at% Fe films due to greater photon absorption efficiency and higher charge-carrier photo-excitation rates. Figure 11 (c) reveals the plot of the Imaginary Dielectric Constant (ε_2)versus wavelength Representing the optical energy loss per cycle due to dipolar absorption. The peak value increases and red-shifts, indicating enhanced intra-band and inter-band transition probabilities in the doped host matrix. Figure 11 (d) reveals the plot of the Optical Dissipation Factor ($\tan\delta$) versus wavelength Reflecting internal optical attenuation and dielectric energy loss. The overall loss factor increases with Fe doping due to free-carrier scattering and localized defect state transition.

This research systematically examined the influence of iron (Fe) doping (0.0, 2.5, 5.0,7.5 and 10.0 at%) on the structural, morphological, and optical characteristics of cobalt oxide (CoO) thin films synthesized via chemical spray pyrolysis.

i. ***Structural & Morphological Effects:*** XRD analysis verified a pure cubic rock-salt phase across all compositions. The substitutional incorporation of larger Fe^{2+} ions (0.780 AA) into host Co^{2+} sites (0.745 AA) expanded the lattice parameter from 4.251 AA to 4.278AA. Higher Fe concentrations led to grain refinement (crystallite size decreased from 28.4 nm to 18.2 nm) and elevated crystal distortion, as indicated by decreases in microstrain ($\varepsilon = 1.22 \times 10^{-3} \rightarrow 1.91 \times 10^{-3}$), dislocation density ($\delta = 1.24 \times 10^{14} \rightarrow 3.02 \times 10^{14}$ lines/m^2).

ii. ***Optical & Dielectric Modifications:*** Optical bandgap energy narrowed significantly from 2.65 eV to 2.05 eV, accompanied by a broadening of the Urbach energy tail ($E_u = 210$ meV $\rightarrow$ 450 meV), confirming heightened structural disorder and localized band-tail state formation. Dispersion properties showed marked enhancement, including an increased refractive index ($n = 2.18 \rightarrow 2.55$ at 600 nm), peak optical conductivity ($\sigma_{opt} = 2.65 \times 10^{14}$ s^{-1}), real dielectric constant ($\varepsilon_1 = 4.91 \rightarrow 6.74$), and dissipation loss factor ($\tan\delta = 0.285 \rightarrow 0.343$).

CONCLUSION

Fe-doping via spray pyrolysis serves as an effective strategy for tuning the structural order, energy band alignment, and optical-dielectric constants of CoO thin films. The ability to shift the absorption edge deep into the visible spectrum while enhancing optical conductivity and dielectric polarizability makes these modified films strong candidates for photovoltaic absorbers, electrochromic devices, and optoelectronic sensors.

REFERENCES

Abeer, K., & Jamal, M. (2023). Bandgap engineering and optical characterizations of modified metal oxide thin films prepared via laser ablation. *Journal of Applied Physics*, 133(8), https://doi.org/085301 .

Akl, A. A., Hassanien, A. S., & Sharma, P. (2021). Microstructural analysis and crystal strain evolution in transition metal-doped oxide coatings. *Applied Physics A*, 127(4), https://doi.org/289–301.

Al-Dahaan, S. A. J., Al-Khayatt, A. H. O., & Salman, M. K. (2020). Optical dispersion and bandgap characteristics of sprayed iron oxide nanostructured films. *Journal of Physics: Condensed Matter*, 32(14), https://doi.org/145701.

Basith, N. M., Ahsan, M., & Rahman, F. (2021). Electronic structure and dielectric modeling of transition metal-doped oxide semiconductors. *Materials Science in Semiconductor Processing*, 123, https://doi.org/105540.

Borah, J. P., & Sarma, K. C. (2021). Structural evolution and optical enhancement in nanostructured oxide thin films deposited via physical methods. *Thin Solid Films*, 718, https://doi.org/138480.

Chafi, F. Z., Bahmad, L., Hassanain, N., Fares, B., Laanab, L., & Mzerd, A. (2022). Characterization techniques of Fe-doped oxide thin films deposited by the spray pyrolysis method. *Journal of Materials Research and Technology*, 18, https://doi.org/2410–2422

Fares, B., Laanab, L., & Mzerd, A. (2022). Nucleation kinetics and structural properties of transition metal oxides prepared via pneumatic spray pyrolysis. *Surface and Coatings Technology*, 432, https://doi.org/128050.

Hassan, N., Chafi, F. Z., & Bahmad, L. (2022). Optimization of deposition parameters in chemical spray pyrolysis for functional oxide films. *Materials Today Communications*, 31, https://doi.org/103290.

Hassanien, A. S., & Akl, A. A. (2020). Microstructure and crystal distortion parameters of sprayed inorganic thin films. *Journal of Non-Crystalline Solids*, 530, https://doi.org/119790.

Mahmood, A., Fatima, N., & Khan, M. A. (2022). Substrate temperature and dopant effects on optical bandgap shifts in transition metal oxide thin films. *Optical Materials*, 125, https://doi.org/112080.

Mariño-Otero, T., Oliver-Tolentino, M., & Aguilar-Frutis, M. A. (2020). Synthesis and photo-electrochemical evaluation of spray-pyrolyzed hematite thin films. *International Journal of Hydrogen Energy*, 45(11), https://doi.org/6210–6218.

Mzerd, A., Bahmad, L., & Chafi, F. Z. (2022). Physical and optical properties of doped cobalt and copper oxides for renewable energy applications. *Solar Energy Materials and Solar Cells*, 238, https://doi.org/111610.

Oral, A. Y., Mensur, E., & Aslan, M. (2021). Optical absorption mechanisms and sp-d exchange interactions in iron-doped p-type oxide semiconductors. *Physica B: Condensed Matter*, 602, https://doi.org/412580.

Patil, S. P., Orlova, T., & Petrov, V. (2022). Functional transition metal oxide thin films: Growth, characterization, and device integration. *Progress in Materials Science*, https://doi.org/126,100920.

Reguera, E., Pérez-Cappe, E., & Contreras-Martínez, G. (2021). Structural stability and catalytic properties of cobalt-based oxide thin films. *ACS Applied Materials & Interfaces*, 13(18), https://doi.org/21340–21350.

Sahay, P. P., Tiwari, S., & Jha, S. (2021). Synthesis and gas sensing properties of iron-doped oxide nanostructures. *Sensors and Actuators B: Chemical*, 330, https://doi.org/129340.

Sarma, K. C., Borah, J. P., & Nath, P. (2023). Doping-induced strain and structural phase transformations in sprayed oxide thin films. *Journal of Alloys and Compounds*, 938, https://doi.org/168590.

©2026 This is an Open Access article distributed under the terms of the Creative Commons Attribution 4.0 International license viewed via https://creativecommons.org/licenses/by/4.0/ which permits unrestricted use, distribution, and reproduction in any medium, provided the original work is cited appropriately.